Journal of Materials Chemistry A

ROYAL SOCIETY OF CHEMISTRY

PAPER

View Article Online
View Journal

Cite this: DOI: 10.1039/d6ta00851h

Dual-axis interfacial engineering of carbon paper hosts for stable anode-less lithium metal batteries

Sangjin Bae,†[ab] Gaeun Park,†[a] Jihwan Byun,[a] Jisub Kim,[a] Jongmin Won,[ab] Sujin Kim,[b] Minjun Je,[a] Heemin Kim,[b] Juhun Shin,[b] Jongseok Moon,[b] Jihoon Oh *[ac] and Jang Wook Choi *[acd]

Received 28th January 2026
Accepted 31st March 2026

DOI: 10.1039/d6ta00851h

rsc.li/materials-a

Anode-less lithium (Li) metal batteries (LMBs) offer exceptional energy density but suffer from rapid capacity degradation caused by unstable Li plating and electrolyte decomposition on bare current collectors. Here, we address these challenges using a dual-functionalized three-dimensional (3D) carbon paper (CP) host. We convert the inherent PTFE coating of commercial CP into an inorganic pre-formed solid electrolyte interphase (pre-SEI) while simultaneously integrating lithiophilic MgO nanoparticles *via* a single-step co-annealing process, creating a MgO-preSEI-CP composite. The pre-SEI layer passivates the interface and suppresses parasitic reactions, while MgO nanoparticles provide uniformly distributed nucleation sites that enhance surface lithiophilicity. By simultaneously reducing electronic conductivity at the surface and improving electrolyte wettability, this dual-functional design establishes an internal potential gradient, directing Li plating into the host interior rather than forming surface dendrites. This synergistic approach demonstrates a generalizable design strategy for 3D hosts that enable stable operation of anode-less LMBs.

Introduction

Rechargeable lithium (Li) metal batteries (LMBs) are regarded as a leading next-generation energy-storage technology, driven by the exceptional theoretical capacity (3860 mAh g^{-1}) and the lowest electrochemical potential (−3.04 V *vs.* NHE) of the Li metal anode.[1–5] These intrinsic properties promise energy densities surpassing those of conventional Li-ion systems, galvanizing research into stabilizing Li metal anodes.[6–9]

Among LMB configurations, the anode-less design—where the cell is assembled without Li metal and all active Li is plated from the cathode during charging—has gained prominence for maximizing gravimetric and volumetric energy density.[10–13] Paradoxically, this very advantage introduces a critical vulnerability: the absence of excess Li renders the anode interface profoundly fragile.[14,15] During cycling, inhomogeneous Li nucleation on bare current collectors leads to mossy and dendritic growth, producing electrically isolated dead Li.[16,17] Simultaneously, the constantly evolving high-surface-area deposit promotes continuous electrolyte reduction and uncontrolled solid electrolyte interphase (SEI) growth.[18–20] The irreversible accumulation of dead Li coupled with a thickening SEI culminates in rapid capacity fade.[21,22] This degradation mechanism is particularly catastrophic in anode-less systems, where the Li inventory is strictly limited and irreplaceable. Therefore, achieving uniform Li deposition and mitigating parasitic interfacial reactions are fundamental prerequisites for realizing practical anode-less LMBs.

To address these challenges, host-assisted Li storage has emerged as an effective strategy to physically regulate deposition and homogenize nucleation.[23–25] Among various architectures, three-dimensional (3D) porous carbon frameworks offer distinct advantages: they provide continuous conductive networks, high internal surface area, and substantial pore volume to spatially accommodate plated Li.[26,27] By distributing nucleation sites across a 3D matrix rather than concentrating them on a planar surface, such hosts lower the local current density and promote inward, uniform Li growth.[28–30]

In this context, commercial carbon paper (CP) presents an appealing host candidate, characterized by a mechanically robust, interconnected fibrous network and significant internal void space (Fig. 1a).[31] However, most commercially available CPs are engineered as gas-diffusion layers and consequently incorporate a polytetrafluoroethylene (PTFE) coating.[32] When employed directly as an anode host, this PTFE coating undergoes irreversible electrochemical reduction during initial lithiation, irreversibly consuming active Li and severely compromising the initial coulombic efficiency (ICE).[33,34] In this work, we introduce a strategy that exploits the inherent PTFE coating of 3D CP host by thermochemically converting it,

[a]*School of Chemical and Biological Engineering, Institute of Chemical Process, Seoul National University, Seoul 08826, Republic of Korea. E-mail: jangwookchoi@snu.ac.kr*

[b]*R&D Center, Samsung SDI, Suwon-si 16678, Republic of Korea*

[c]*Institute for Battery Research Innovation (IBRI), Seoul National University, Seoul 08826, Republic of Korea. E-mail: jm9731@snu.ac.kr*

[d]*Seoul National University Energy Initiative (SNUEI), Seoul National University, Seoul 08826, Republic of Korea*

† These authors contributed equally.

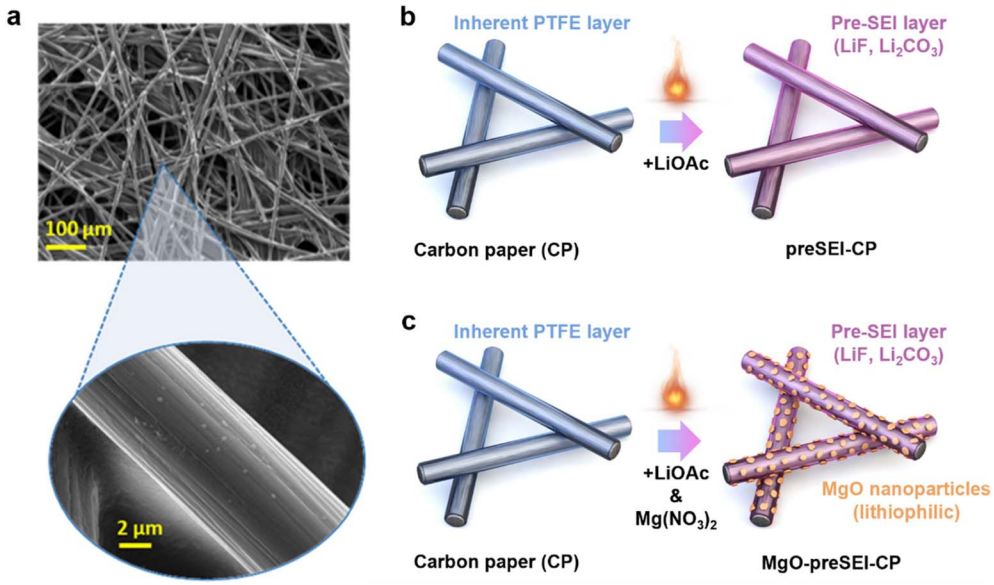

Fig. 1 (a) SEM image of the pristine carbon paper (CP). Schematic illustrations of the preparation process for (b) preSEI-CP and (c) MgO-preSEI-CP.

together with lithium acetate, into a robust inorganic pre-formed SEI (pre-SEI) of LiF and Li_2CO_3 prior to cycling (Fig. 1b). This layer suppresses initial PTFE decomposition and mitigates subsequent electrolyte reduction. Additionally, to address the intrinsic lithiophobicity of the carbon fiber, we co-integrated magnesium oxide (MgO) as stable lithiophilic seeds through a single-step annealing process using $Mg(NO_3)_2$ as a precursor (Fig. 1c).[35,36] The resulting MgO-preSEI-CP composite thus exhibits a dual-functional architecture: the pre-SEI layer conserves Li and passivates the interface, while the MgO nanoparticles guide uniform Li nucleation and deposition.

Electrochemical analysis confirmed that MgO-preSEI-CP lowers polarization, stabilizes interfacial resistance, and promotes dense Li infilling. In an anode-less full cell, it sustains 80% capacity retention over 85 cycles. This approach concurrently tackles two key degradation pathways—continuous SEI growth and dead Li accumulation—by integrating a protective pre-SEI with fixed lithiophilic nucleation sites within a 3D host.

Results and discussion

The pristine CP substrate is composed of interconnected, straight carbon fibers with substantial internal porosity. Consistent with its commercial source, energy-dispersive X-ray spectroscopy (EDS) and X-ray photoelectron spectroscopy (XPS) analyses confirmed a surface PTFE coating. EDS mapping revealed a uniform fluorine distribution across the fibers (Fig. S1), while XPS identified characteristic C–F_2 bonding states in the C 1s and F 1s spectra (Fig. S2). When employed as an anode, this pristine CP exhibited a pronounced voltage plateau near 0.7 V (*vs.* Li/Li^+) during initial lithiation (Fig. S3).[37] This plateau corresponds to the irreversible electrochemical reductive decomposition of the surface PTFE (eqn (1)).

$$(C_2F_4)_n + 4nLi^+ + 4ne^- \rightarrow 2nC\ (amorphous) + 4nLiF \quad (1)$$

To mitigate this loss, a thermally driven pre-treatment strategy was developed to convert the PTFE coating into a beneficial artificial pre-SEI. In this process, PTFE reacts with infiltrated lithium acetate (LiOAc), generating LiF and Li_2CO_3 (from LiOAc self-decomposition) during annealing.[38,39] Thermally, LiOAc decomposes near 350 °C to form Li_2CO_3, while PTFE begins to decompose in air at approximately 400 °C, yielding CO_2 (g) and HF (g).[40] The *in situ* generated Li_2CO_3 subsequently reacts with HF (g) to produce LiF *via* the following reaction pathway (eqn (2)–(4))[41,42]

$$2Li(CH_3COO) \rightarrow \mathbf{Li_2CO_3} + (CH_3)_2CO\ (g)\ (>350\ ^\circ C) \quad (2)$$

$$-(CF_2–CF_2)_n- + 2nH_2O + nO_2 \rightarrow 2nCO_2 + 4n\mathbf{HF}\ (g)\ (>400\ ^\circ C) \quad (3)$$

$$Li_2CO_3 + 2HF\ (g) \rightarrow 2\mathbf{LiF}\ (s) + CO_2\ (g) + H_2O\ (g) \quad (4)$$

The resulting host (denoted as preSEI-CP) was characterized to determine the composition and distribution of the reaction products. SEM and EDS mapping confirmed that the fibrous architecture remained intact after treatment, with fluorine and oxygen uniformly dispersed across the carbon network (Fig. 2a). XPS analysis identified signatures of residual CF_x, LiF, and Li_2CO_3 (Fig. 2b). The formation of crystalline LiF and Li_2CO_3 was further corroborated by XRD (Fig. S4), which also showed the complete disappearance of the characteristic PTFE diffraction peak at 18.1°.

The electrochemical impact of this pre-formed SEI was evaluated using the initial lithiation voltage profile in half-cells (Fig. 2c). In the preSEI-CP electrode, the characteristic 0.7 V plateau corresponding to PTFE reduction was entirely eliminated. Concurrently, the ICE increased markedly to 93.3% from 83.9% of bare CP. This enhancement is directly attributed to the

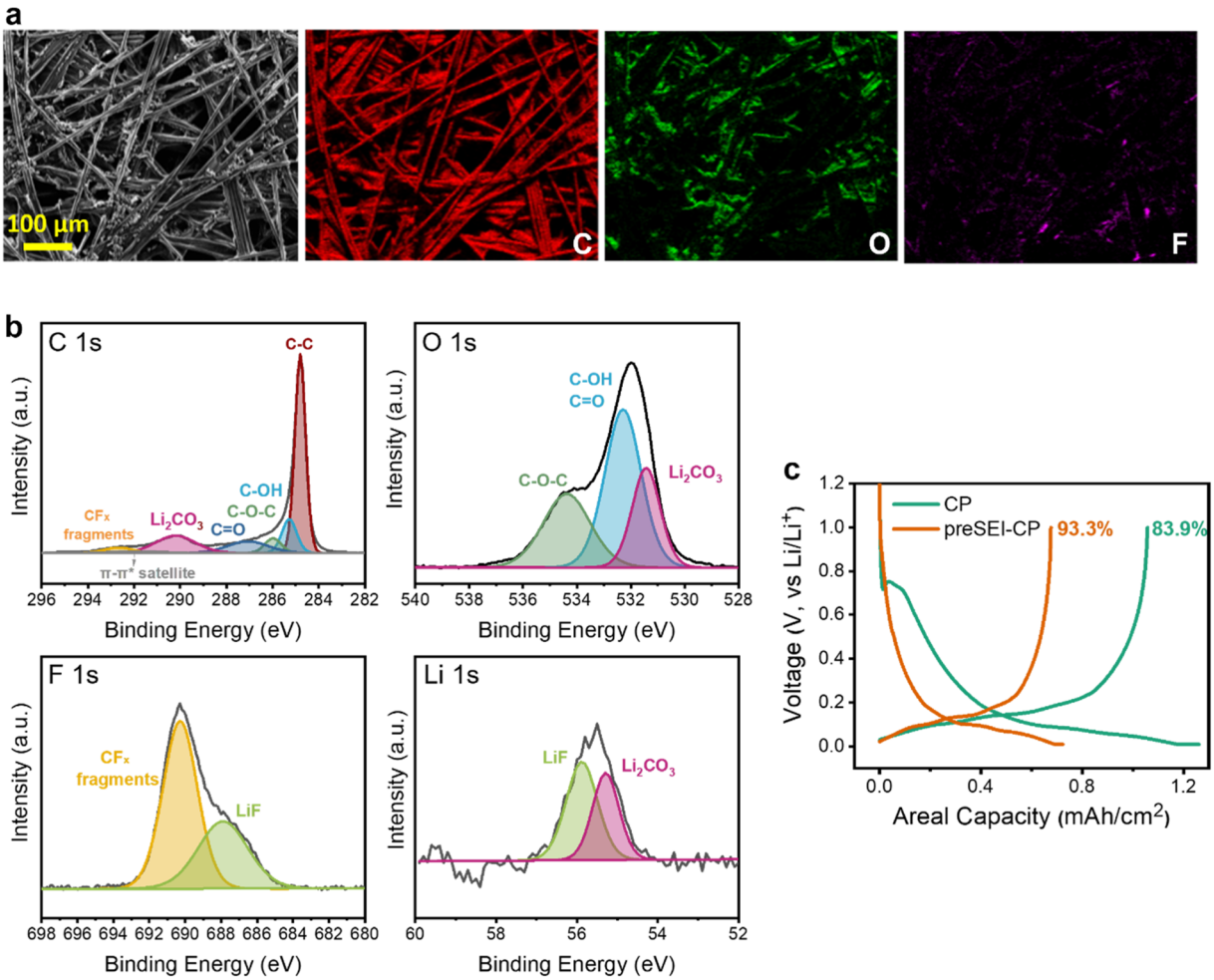

Fig. 2 (a) SEM image and corresponding EDS elemental maps of preSEI-CP. (b) High-resolution XPS spectra of preSEI-CP. (c) First-cycle voltage profiles of pristine CP and preSEI-CP in half-cells.

prior thermochemical conversion of PTFE and the presence of a stable, inorganic pre-SEI, which effectively minimizes parasitic electrolyte decomposition during the first cycle. The residual CF_x fragments in preSEI-CP appear electrochemically inactive, likely due to loss of crystallinity and fragmentation into short-chain species embedded within the carbon matrix, thereby eliminating the electrochemical activity characteristic of crystalline PTFE.

While a pre-formed SEI stabilizes the interface, enhancing the electrode's lithiophilicity—governing where Li^+ ions reduce and nucleate—is crucial for long-term cyclability by enabling homogeneous Li nucleation and growth.[43] In CP, Li storage follows a sequence: (1) intercalation into graphitic domains, (2) plating on fiber surfaces, and (3) pore filling (Fig. S5). Step (2) is most critical, as initial plating dictates subsequent growth morphology.[44] To directly enhance lithiophilicity at this stage, MgO nanoparticles were introduced during pre-SEI formation owing to its lithiophilic nature and, critically, its non-alloying character. This ensures structural and chemical stability during repeated plating/stripping cycles—a key advantage over metallic alloying seeds, which are prone to mechanical fracture and physical detachment as a result of continuous alloying/dealloying with Li.[45] Magnesium nitrate ($Mg(NO_3)_2$) was chosen as the precursor, decomposing thermally to MgO upon annealing (eqn (5)).

$$2Mg(NO_3)_2 \rightarrow 2MgO\ (s) + 4NO_2\ (g) + O_2\ (g) \quad (5)$$

The characterization of MgO-preSEI-CP confirmed the integration and distribution of MgO nanoparticles within the pre-SEI matrix. XPS revealed new MgO signatures in the O 1s and Mg 1s regions, alongside the characteristic LiF and Li_2CO_3 peaks (Fig. 3a). Notably, residual CF_x signals present in preSEI-CP were absent, likely due to complete oxidation of PTFE fragments by the NO_2 and O_2 released during $Mg(NO_3)_2$ decomposition.[46] Crystalline MgO was further verified by XRD (Fig. S6). SEM/EDS mapping showed uniform Mg distribution across the CP (Fig. 3b) and on individual fibers (Fig. S7), confirming homogeneous surface modification. Raman spectroscopy indicated a progressive increase in structural defects, with the D/G ratio rising from 0.16 (pristine CP) to 0.59 (preSEI-CP) and to 0.73 (MgO-preSEI-CP) (Fig. 3c). This trend suggests chemical coupling between the carbon framework and the in situ-formed

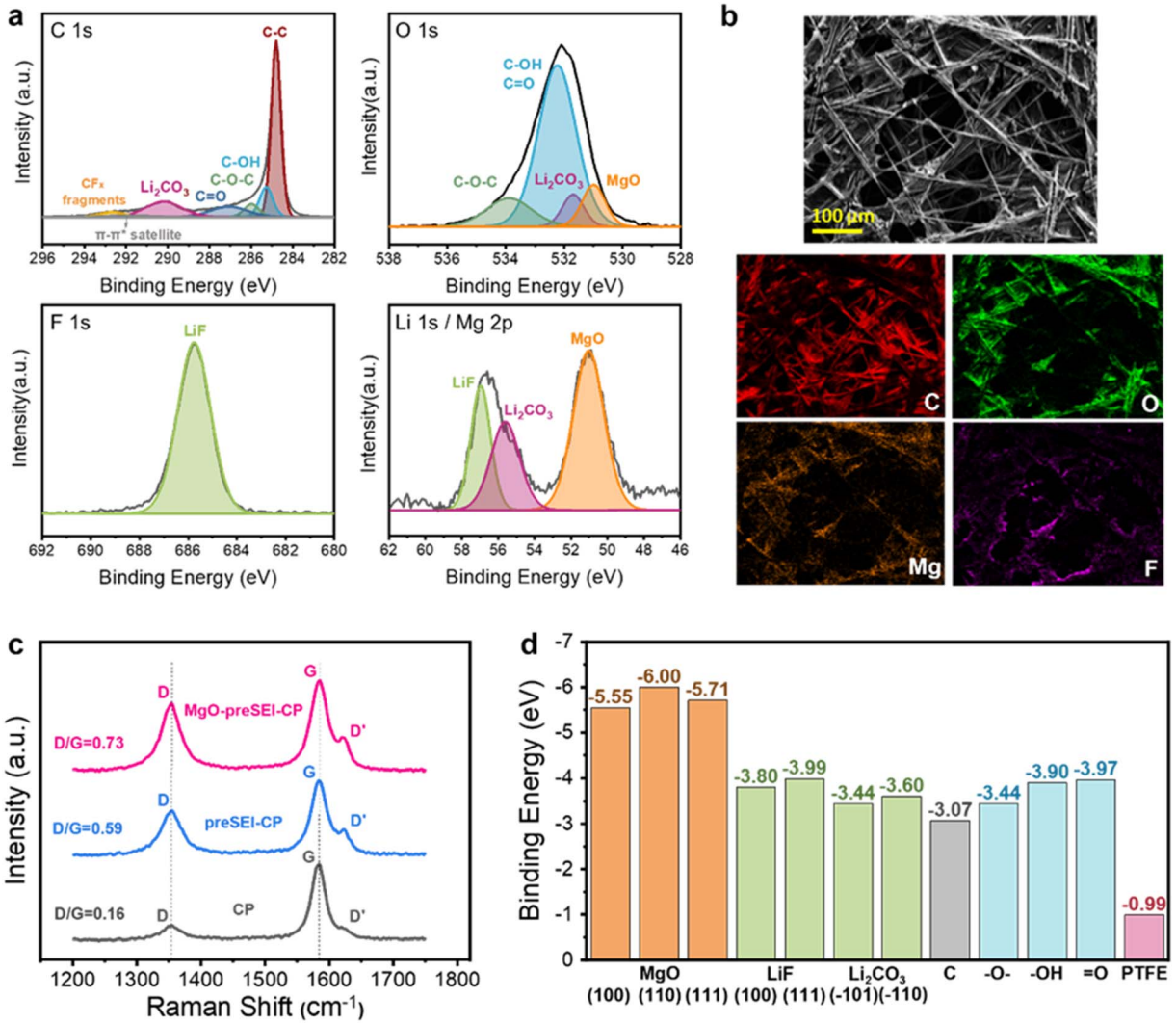

Fig. 3 (a) High-resolution XPS spectra for MgO-preSEI-CP. (b) SEM image and corresponding EDS elemental mappings of MgO-preSEI-CP. (c) Raman spectra of CP, preSEI-CP, and MgO-preSEI-CP, together with the corresponding D/G ratios. (d) DFT-calculated Li^+ binding energies on various surface sites existing in CP-based host materials.

SEI components, with MgO integration further increasing the sp^3 fraction.

Density functional theory (DFT) calculations were performed to evaluate MgO as a Li nucleation seed by comparing the relative binding energies of unsolvated Li^+ on relevant surfaces (Fig. 3d and S8). Li^+ exhibited the weakest interaction with PTFE (−0.99 eV), followed by graphitic carbon (−3.07 eV), confirming the intrinsic lithiophobicity of pristine CP. Binding strengthened moderately on oxidized carbon functionalities (–O–: −3.44 eV, –OH: −3.90 eV, ═O: −3.97 eV) and on pre-SEI components of LiF (−3.80 to −3.99 eV) and Li_2CO_3 (−3.44 to −3.60 eV), indicating that pre-SEI formation partially improves substrate lithiophilicity. Furthermore, Li^+ binding was substantially stronger on all MgO facets in MgO-preSEI-CP, with energies of −5.55 eV (100), −6.00 eV (110), and −5.71 eV (111). Although these calculations are based on relative trends and do not account for a sophisticated solvation or electrolyte environment, they unequivocally demonstrate that dispersed MgO nanoparticles provide highly lithiophilic sites, capable of strongly attracting Li^+ and guiding preferential Li nucleation.

The initial Li deposition morphology on each host was examined using SEM after depositing 1.0 mAh cm^{-2} (Fig. S9). Pristine CP and preSEI-CP exhibited rough, mossy Li, indicating non-uniform nucleation. In contrast, MgO-preSEI-CP showed a compact, conformal Li layer uniformly coating the fibers, consistent with the strong Li^+ adsorption on MgO predicted by DFT and confirming its role as an effective nucleation seed.

Voltage profiles from the first and second cycles were compared to assess the electrochemical impact of MgO. The formation cycle for MgO-preSEI-CP (Fig. 4a) revealed no additional parasitic reactions, with ICE similar to preSEI-CP, indicating MgO incorporation does not disrupt SEI formation. This is supported by nearly identical cycling voltammetry (CV) profiles for preSEI-CP and MgO-preSEI-CP (Fig. S10).

Polarization during the second deposition cycle was lowest for MgO-preSEI-CP (Fig. 4b). Nucleation/plating overpotentials,

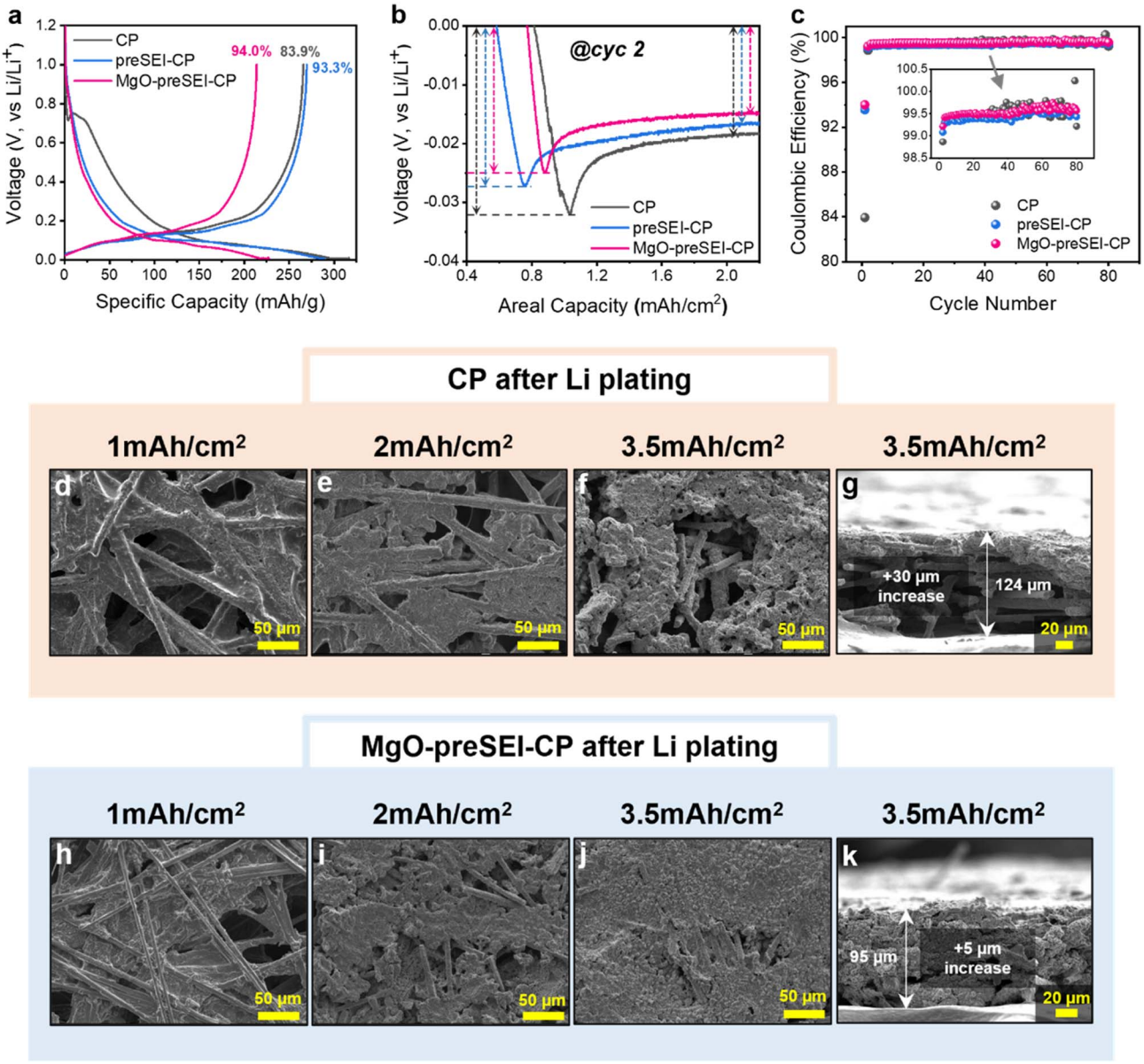

Fig. 4 (a) Voltage profiles in half-cells during the initial Li plating/stripping cycle. (b) Nucleation overpotentials and steady-state plating overpotentials observed at the 2nd plating cycle in half-cells. (c) Li plating/stripping CEs in half-cells. (d–k) SEM images of the host morphology after Li deposition at different areal capacities: (d–g) CP at 1, 2, and 3.5 mAh cm^{-2} and the corresponding cross-sectional view at 3.5 mAh cm^{-2}. (h–k) MgO-preSEI-CP at 1, 2, and 3.5 mAh cm^{-2} and the corresponding cross-sectional view at 3.5 mAh cm^{-2}.

defined as the minimum voltage point and the point of minimal voltage variation (at 2.2 mAh cm^{-2}) during Li plating, respectively, were largest for pristine CP (−32.1/−18.4 mV), reduced for preSEI-CP (−27.3/−16.6 mV), and lowest for MgO-preSEI-CP (−25.1/−14.7 mV), attributed to MgO's strong lithiophilicity. Consequently, MgO-preSEI-CP achieved the highest average CE over 80 cycles (99.47%) during repeated Li plating/stripping evaluation, outperforming preSEI-CP (99.37%) and pristine CP (99.32%) (Fig. 4c).

To compare Li storage mechanisms, we monitored deposition morphology evolution in MgO-preSEI-CP and pristine CP from 1.0 to 3.5 mAh cm^{-2} (at 0.5 mA cm^{-2}) after formation cycle (Fig. 4d–k). At low capacities (1–2 mAh cm^{-2}), both hosts showed similar plating within inter-fiber spaces (Fig. 4d, e, h and i). A clear divergence emerged at 3.5 mAh cm^{-2}: MgO-preSEI-CP exhibited conformal, uniform growth along fibers and gradual pore filling, while CP showed preferential Li accumulation near the top surface (Fig. 4f and j). Cross-sectional images revealed dense Li confined to the upper region in CP, leaving internal pores largely unfilled (Fig. 4g), whereas MgO-preSEI-CP enabled uniform Li penetration throughout the 3D framework (Fig. 4k). Consequently, CP expanded by 30 μm relative to its pristine state, compared to only 5 μm for MgO-preSEI-CP (Fig. S11). These findings indicate that MgO not only promotes conformal coating on individual fibers but also guides uniform, inward Li deposition at higher

capacities. This trend remained consistent at both mild (0.5 mA cm^{-2}) and high (2.0 mA cm^{-2}) current densities (Fig. S12), confirming the robustness of the proposed host engineering under demanding high-rate cycling conditions.

The uniform, inward Li deposition in MgO-preSEI-CP arises from factors beyond lithiophilicity alone, including modified electrical conductivity and enhanced electrolyte wettability. First, the thermochemical incorporation of inorganic components reduces the host's electrical conductivity. Two-probe measurements (1 cm spacing, Fig. S13) showed the highest resistance for MgO-preSEI-CP (13.3 Ω), followed by preSEI-CP (9.8 Ω), and the lowest for pristine CP (2.5 Ω). Through-plane resistance followed the same trend (Fig. S14): MgO-preSEI-CP (0.362 Ω) > preSEI-CP (0.284 Ω) > CP (0.125 Ω). These results align with the increasing D/G ratios from Raman spectroscopy, which indicate a lower fraction of conductive graphitic domains. Apparent conductivities, estimated from through-plane data, were 0.79 S m^{-1} (MgO-preSEI-CP), 0.90 S m^{-1} (preSEI-CP), and 2.39 S m^{-1} (CP). Given the porous architecture, these values should be interpreted relatively: MgO-preSEI-CP and preSEI-CP retain approximately 33% and 38%, respectively, of the conductivity of pristine CP (normalized to 100%).

Second, electrolyte wettability is markedly improved by the inorganic composite layer. Wettability was assessed by measuring the weight gain after a 20 s immersion in the cycling electrolyte (3 M LiFSI in FSA; Fig. S15). Both preSEI-CP and MgO-preSEI-CP absorbed significantly more electrolyte (~1024% and ~1056% weight increase, respectively) compared to pristine CP (~443%). This enhancement is attributed to the ionic nature of the incorporated inorganic phases (LiF, Li_2CO_3, and MgO), which are inherently more compatible with polar electrolytes. The higher uptake for MgO-preSEI-CP may be further promoted by the strong Li^+ affinity of MgO, which attracts solvated Li^+ species to the surface.

To further examine the wetting behavior, contact angle measurements were performed by dispensing 20 μL of electrolyte onto each electrode surface (Fig. S16). Pristine CP exhibited a contact angle of 54°, whereas both preSEI-CP and MgO-preSEI-CP showed an apparent contact angle of 0°, with the droplets being immediately absorbed upon contact. These observations confirm the markedly improved electrolyte wettability of the engineered hosts compared with pristine CP.

To elucidate how these electrical conductivity and electrolyte wettability jointly influence Li deposition behavior within the host framework, it is instructive to consider the spatial profiles of electrical potential and electrolyte availability along the host thickness (Fig. 5a). The local current density, $J_s(x)$, can be described as:

$$J_s(x) = -\sigma_s \frac{d\Phi}{dx} \quad (6)$$

which, upon integration with respect to x, yields:

$$J_n = -\sigma_s \frac{(\Phi_L - \Phi_0)}{L} \quad (7)$$

where J_n denotes the bulk current density, which remains constant under constant-current (CC) conditions, σ_s is the electrical conductivity of the host material, Φ_x represents the electrical potential at position x, and L is the thickness of the host material. In this treatment, the host framework is approximated as a homogeneous electronic conductor with an effective conductivity (σ_s), and current flow is assumed to occur predominantly along the thickness direction under steady-state CC operation. Accordingly, this simplified analysis focuses on the distribution of electronic potential within the host, while ionic transport in the electrolyte-filled pores and charge-transfer kinetics at the Li/electrolyte interface are not explicitly considered.

Consequently, the electrical potential drop ($\Phi_L - \Phi_0$) across the host thickness depends on its conductivity. Lower conductivity in MgO-preSEI-CP creates the steepest potential gradient, leading to a much lower electrical potential at the bottom ($x = 0$) compared to the surface ($x = L$), which results in a larger local overpotential in the interior. This promotes charge-transfer reactions preferentially within the host for more facile Li plating therein. Electrolyte availability also varies spatially with wettability. Poorly wettable CP confines most electrolyte near the surface, concentrating Li^+ reduction there. In contrast, the excellent wettability of MgO-preSEI-CP enabled uniform electrolyte penetration, supplying Li^+ homogeneously throughout the fiber network. Together, the steep internal potential gradient and uniform electrolyte access drive Li deposition inward, explaining the markedly deeper growth in MgO-preSEI-CP *versus* pristine CP.

This framework similarly governs the initial deposition behavior of preSEI-CP. When plating 3.5 mAh cm^{-2} of Li, preSEI-CP exhibited minimal expansion (~4 μm) and pronounced inward deposition, analogous to MgO-preSEI-CP (Fig. S17). Although preSEI-CP possesses marginally higher conductivity and slightly lower electrolyte uptake than MgO-preSEI-CP, both hosts exhibited similar inward-deposition behavior during initial Li plating. This is once again driven by a local potential gradient and sufficient electrolyte penetration, which is clearly distinct from the surface-dominated plating observed on pristine CP.

However, a critical divergence emerged upon long-term cycling. Cross-sectional SEM analysis after the 81st deposition revealed that Li deposition in preSEI-CP progressively shifted toward the top surfaces, resembling surface-dominated plating on pristine CP, whereas MgO-preSEI-CP continued to exhibit pronounced inward Li growth. Consistently, MgO-preSEI-CP maintained the smallest host thickness expansion among all samples, which was substantially lower than that of preSEI-CP (Fig. S18). This indicates that while the potential gradient in preSEI-CP can initially induce inward plating, sustained, stable cycling necessitates a more lithiophilic host. The incorporation of MgO is therefore desirable for promoting consistent inward deposition and ensuring long-term plating–stripping stability. The durability of the MgO modification was further evidenced by SEM/EDS after 80 cycles (stripped state, Fig. S19). The nanoparticles retained a fine dispersion and remained firmly anchored to the carbon fibers, closely matching their pre-cycling distribution. No signs of detachment or agglomeration were observed, highlighting the robust mechanical and spatial

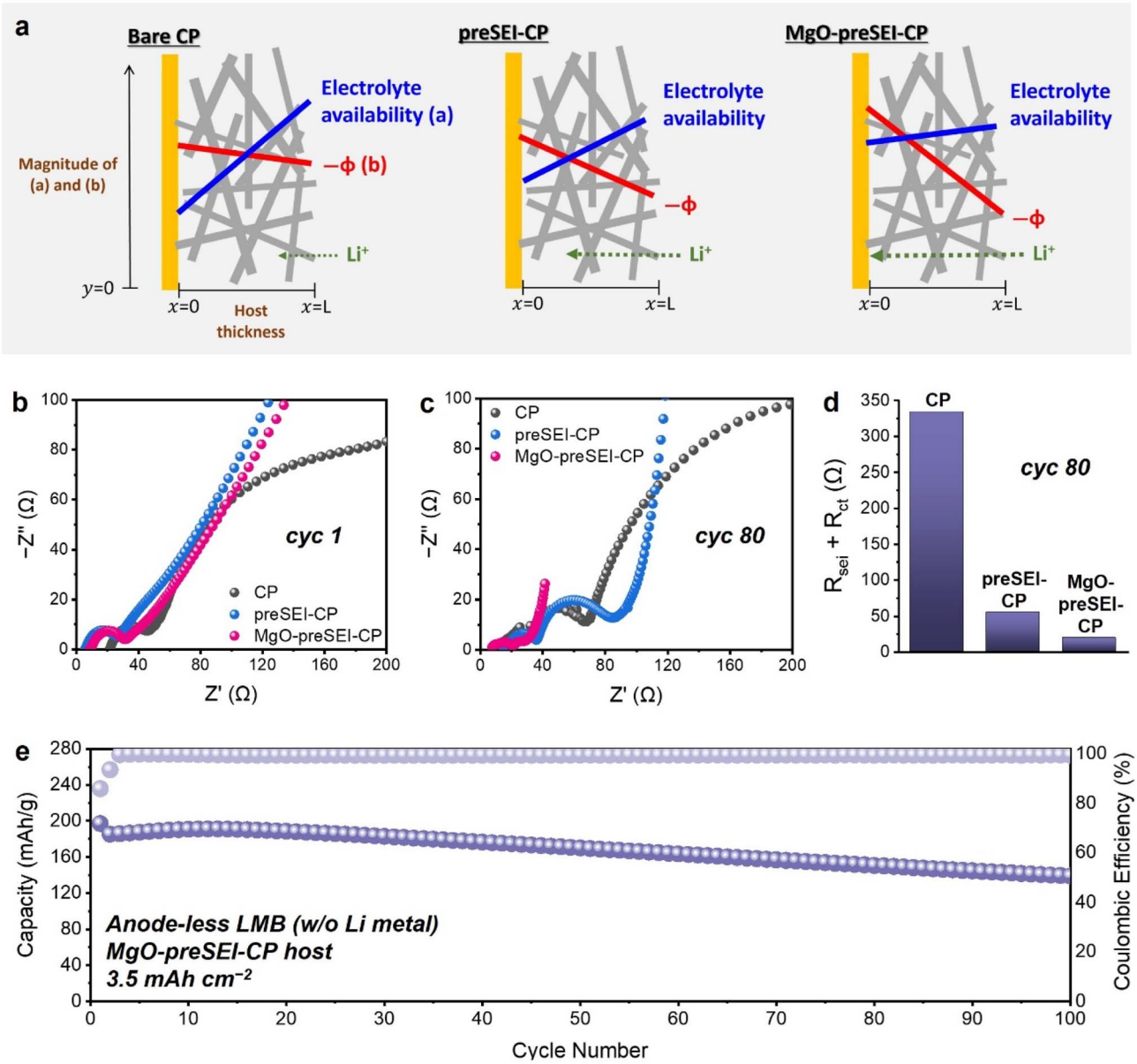

Fig. 5 (a) Schematic illustration of the relative spatial profiles of electrical potential and electrolyte availability across the host thickness for CP, preSEI-CP, and MgO-preSEI-CP. (b and c) EIS Nyquist plots of half-cells after the (b) 1st and (c) 80th cycles. (d) R_{sei} + R_{ct} values after 80 cycles calculated with the fitting circuit. (e) Cycling performance of anode-less full cells employing an NCM811 cathode (3.5 mAh cm^{-2}) with MgO-preSEI-CP as the anode-less host material.

immobilization of these non-alloying sites during extended cycling.

To evaluate how Li deposition behavior affects interfacial stability, electrochemical impedance spectroscopy (EIS) was performed after the 1st and 80th cycles (Fig. 5b, c and S20). Pristine CP showed the highest interfacial resistance—defined as the sum of SEI resistance (R_{sei}) and charge-transfer resistance (R_{ct})—initially (237.7 Ω) and the largest increase by the 80th cycle (+96.7 Ω to 334.4 Ω). In contrast, initial resistance was markedly lower for preSEI-CP (18.6 Ω) and MgO-preSEI-CP (22.8 Ω). While preSEI-CP resistance increased significantly to 54.6 Ω after 80 cycles, MgO-preSEI-CP exhibited exceptional stability, maintaining a nearly identical resistance of 18.9 Ω (Fig. 5d). This stability is attributed to MgO-preSEI-CP's uniform Li growth on fibers and inward-dominant deposition, which collectively minimize continuous SEI reformation and dead Li formation.

The full-cell cycling performance of the three hosts was evaluated in an anode-less configuration, paired with an NCM811 cathode (3.5 mAh cm^{-2}) without excess Li metal (Fig. 5e and S21). With no initial Li source, the N/P ratio is effectively 0—and even if the CP host's intercalation capacity is considered as an anode active material, the ratio remains only 0.25—confirming that the system operates in an anode-less configuration. Pristine CP showed the poorest initial reversibility (ICE_{CP} = 76.7%), reaching 80% capacity retention after only 63 cycles. The preSEI-CP host

exhibited improved early-cycle reversibility due to its pre-formed SEI ($ICE_{preSEI\text{-}CP}$ = 86.9%), but its capacity decayed rapidly in mid-cycling due to insufficient lithiophilic regulation, converging toward CP's performance (80% retention at 68 cycles). In contrast, MgO-preSEI-CP delivered markedly enhanced cycling stability ($ICE_{MgO\text{-}preSEI\text{-}CP}$ = 85.9%), maintaining 80% capacity retention for 85 cycles.

To further compare the electrochemical output relative to host mass, the accumulated capacities over 85 cycles are plotted as a function of the areal mass of the host materials (Fig. S22).[47] Notably, MgO-preSEI-CP delivers the highest accumulated capacity despite having the lowest host mass, further confirming its superior Li reversibility. This performance disparity became increasingly pronounced under high-rate charge–discharge conditions. During rate capability tests conducted over current densities ranging from 0.2C to 3C, the performance gap between the MgO-preSEI-CP and the control sample systematically widened with increasing charge–discharge rates, unequivocally demonstrating the superior rate capability of the MgO-preSEI-CP (Fig. S23). This superior performance underscores the critical role of strongly lithiophilic, spatially fixed nucleation seeds in sustaining long-term cyclability in anode-less architectures, where the Li inventory is strictly cathode-derived and finite.

After 80 cycles, cross-sectional SEM analysis revealed the order of host thickness increase: MgO-preSEI-CP < preSEI-CP < CP, confirming that bottom-growth deposition enabled by host engineering significantly improves long-term cycling stability (Fig. S24). Nevertheless, dead Li remained in the MgO-preSEI-CP sample, albeit to a lesser extent than in the other CP-based hosts—underscoring a critical challenge in anode-less systems, where any Li loss directly translates to capacity decay. Thus, while directing deposition toward the host bottom is beneficial, additional strategies are still needed to further mitigate Li loss in the anode-less configuration.

Conclusions

This study demonstrates how interfacial chemistry and lithiophilicity govern Li deposition behavior and cycling stability in commercial CP-based anode-less LMBs. A composite host (MgO-preSEI-CP) was fabricated through a thermochemical conversion of PTFE into a LiF/Li_2CO_3 pre-SEI, with MgO nanoparticles uniformly integrated *via* co-annealing. The pre-SEI and MgO together enhance surface lithiophilicity for uniform nucleation and, by reducing electronic conductivity while improving electrolyte wettability, promote inward Li deposition. This creates an internal potential gradient and uniform ion supply that direct plating into the host interior, resulting in dense Li filling, minimal electrode expansion, and decent interfacial stability with negligible impedance growth. Our work establishes a dual-axis design principle: a pre-formed inorganic SEI conserves Li by suppressing parasitic reactions, while spatially fixed, non-alloying MgO seeds guide uniform nucleation and growth. This synergistic strategy establishes a generalizable 3D host design for stable, high-energy anode-less batteries operating under Li-limited conditions.

Author contributions

S. B. and J. W. C. conceived the idea and designed the experiments. S. B. and G. P. synthesized samples. J. B. conducted computational simulations. S. B., G. P., J. K., J. W., S. K., and M. J. performed electrochemical experiments. H. K., J. S., and J. M. conducted sample characterizations. S. B., G. P., J. O., and J. W. C. wrote the manuscript. J. O. and J. W. C. supervised the research. All authors discussed the results and contributed to the manuscript preparation.

Conflicts of interest

The authors declare no conflict of interest.

Data availability

All data are available within the manuscript and supplementary information (SI). Supplementary information is available. See DOI: https://doi.org/10.1039/d6ta00851h.

Acknowledgements

This work was supported by the National Research Foundation of Korea (NRF) (Grants RS-2023-00261543 and RS-2024-00464386) and the National Research Council of Science and Technology (NST) (GTL24012-000). J. W. C. also acknowledges support from the Institute of Engineering Research (IOER), the Institute for Battery Research Innovation (IBRI), the SOFT Foundry Institute, and the Research Institute of Advanced Materials (RIAM) at Seoul National University. This work was also supported by Samsung SDI.

References

1 X. Hu, Z. Zhang, X. Zhang, Y. Wang, X. Yang, X. Wang, M. Fayena-Greenstein, H. A. Yehezkel, S. Langford, D. Zhou, B. Li, G. Wang and D. Aurbach, *Nat. Rev. Mater.*, 2024, **9**, 305–320.
2 H. Ji, J. Xiang, Y. Li, M. Zheng, L. Yuan, Y. Liao, L. Du, Z. Li, Z. Xie, K. Huang, X. Lin, Z. Xie, Y. Shen, M. Chen, T. Li, G. Feng, Y. Sun, L. Qie, H. Li, F. Zhang, R. Guo, X. Feng, W. Chen, X. Ai, J. Lu and Y. Huang, *Nature*, 2025, **643**, 1255–1262.
3 M. Je, J. Sung, J. Oh, H. Kim, D. Park, H. Kim, Y. Song, S.-M. Lee, J. W. Choi and S. Park, *Chem. Eng. J.*, 2025, **524**, 169406.
4 W. Deng, X. Yin, W. Bao, X. Zhou, Z. Hu, B. He, B. Qiu, Y. S. Meng and Z. Liu, *Nat. Energy*, 2022, **7**, 1031–1041.
5 X.-B. Cheng, R. Zhang, C.-Z. Zhao and Q. Zhang, *Chem. Rev.*, 2017, **117**, 10403–10473.
6 Z. Li, Y. Chen, X. Yun, P. Gao, C. Zheng and P. Xiao, *Adv. Funct. Mater.*, 2023, **33**, 2300502.
7 Y. Yin, Y. Yang, D. Cheng, M. Mayer, J. Holoubek, W. Li, G. Raghavendran, A. Liu, B. Lu, D. M. Davies, Z. Chen, O. Borodin and Y. S. Meng, *Nat. Energy*, 2022, **7**, 548–559.

8 L. Braks, J. Zhang, A. Forster, P. Fritz, J. Oh, M. El Kazzi, J. W. Choi and A. Coskun, *Angew. Chem., Int. Ed.*, 2024, **63**, e202408238.
9 J. Xiao, Q. Li, Y. Bi, M. Cai, B. Dunn, T. Glossmann, J. Liu, T. Osaka, R. Sugiura, B. Wu, J. Yang, J.-G. Zhang and M. S. Whittingham, *Nat. Energy*, 2020, **5**, 561–568.
10 N. Lee, J. Oh and J. W. Choi, *Mater. Futures*, 2023, **2**, 013502.
11 J. Oh, J. Kim, S. Bae, H. Kim, T. Lee, S. H. Choi, G. Park, S. Ji, K. J. Kim and J. W. Choi, *Adv. Energy Mater.*, 2025, **15**, e02711.
12 S. E. Sandoval, C. G. Haslam, B. S. Vishnugopi, D. W. Liao, J. S. Yoon, S. H. Park, Y. Wang, D. Mitlin, K. B. Hatzell, D. J. Siegel, P. P. Mukherjee, N. P. Dasgupta, J. Sakamoto and M. T. McDowell, *Nat. Mater.*, 2025, **24**, 673–681.
13 S. H. Choi, C. H. Baek, J. Oh, G.-J. Lee, M. Kim, H. Lee, D.-J. Yoo, Y. S. Jung, K. Kim, J.-S. Yu, W. Cho, H. Park and J. W. Choi, *Nat. Commun.*, 2025, **16**, 5871.
14 Y. An, Z. Pei, D. Luan and X. W. Lou, *Sci. Adv.*, 2025, **11**, eadx7124.
15 J. Oh, Y. Sohn and J. W. Choi, *EES Batteries*, 2025, **1**, 566–575.
16 Y. Zhou, P. Wang, K. Wang, X. Fang, W. Li, J. Nai, Y. Liu, Y. Wang, S. Zou, H. Yuan, X. Tao and J. Luo, *Adv. Funct. Mater.*, 2025, **35**, 2424022.
17 J. Oh, T. Lee, N. Lee, Y. Sohn, J. Y. Kim, K. Y. Bae, S. H. Choi and J. W. Choi, *Battery Energy*, 2025, **4**, e70038.
18 Q.-K. Zhang, X.-Q. Zhang, J. Wan, N. Yao, T.-L. Song, J. Xie, L.-P. Hou, M.-Y. Zhou, X. Chen, B.-Q. Li, R. Wen, H.-J. Peng, Q. Zhang and J.-Q. Huang, *Nat. Energy*, 2023, **8**, 725–735.
19 G. Feng, H. Jia, Y. Shi, X. Yang, Y. Liang, M. H. Engelhard, Y. Zhang, C. Yang, K. Xu, Y. Yao, W. Xu and X. Shan, *Nat. Nanotechnol.*, 2023, **18**, 780–789.
20 X. Liu, S. Li, C. Yuan, B. Zheng, G. Cheng, Y. Chen, X. Lu, D. Gu, B. Lv, H. Li, Z. Yan, H. Qian, Y. Zhu, D. Sun, Y. Song and Y. Xiang, *Nature*, 2025, **646**, 102–107.
21 P. Ma, R. Kumar, K.-H. Wang and C. V. Amanchukwu, *Nat. Commun.*, 2025, **16**, 8396.
22 J. Oh, S. H. Choi, J. Y. Kim, J. Lee, T. Lee, N. Lee, T. Lee, Y. Sohn, W. J. Chung, K. Y. Bae, S. Son and J. W. Choi, *Adv. Energy Mater.*, 2023, **13**, 2301508.
23 X. Wang, Z. Chen, K. Jiang, M. Chen and S. Passerini, *Adv. Energy Mater.*, 2024, **14**, 2304229.
24 S. Cho, D. Y. Kim, J.-I. Lee, J. Kang, H. Lee, G. Kim, D.-H. Seo and S. Park, *Adv. Funct. Mater.*, 2022, **32**, 2208629.
25 Y. Liu, J. Sun, X. Hu, Y. Li, H. Du, K. Wang, Z. Du, X. Gong, W. Ai and W. Huang, *Nano Energy*, 2022, **94**, 106883.
26 S. Yu, Z. Wu, J. Holoubek, H. Liu, E. Hopkins, Y. Xiao, X. Xing, M. H. Lee and P. Liu, *Adv. Sci.*, 2022, **9**, 2104829.
27 W. Chen, S. Li, C. Wang, H. Dou and X. Zhang, *Energy Environ. Mater.*, 2023, **6**, e12412.
28 T. Li, S. Gu, L. Chen, L. Zhang, X. Qin, Z. Huang, Y.-B. He, W. Lv and F. Kang, *Small*, 2022, **18**, 2203273.
29 C. Lu, M. Tian, X. Zheng, C. Wei, M. H. Rummeli, P. Strasser and R. Yang, *Chem. Eng. J.*, 2022, **430**, 132722.
30 Y. Wang, J. Tan, Z. Li, L. Ma, Z. Liu, M. Ye and J. Shen, *Energy Storage Mater.*, 2022, **53**, 156–182.
31 T. Gao, C. Xu, R. Li, R. Zhang, B. Wang, X. Jiang, M. Hu, Y. Bando, D. Kong, P. Dai and X.-B. Wang, *ACS Nano*, 2019, **13**, 11901–11911.
32 D. Bevers, R. Rogers and M. von Bradke, *J. Power Sources*, 1996, **63**, 193–201.
33 G. Li, R. Xue and L. Chen, *Solid State Ionics*, 1996, **90**, 221–225.
34 T. Lee, J. An, W. J. Chung, H. Kim, Y. Cho, H. Song, H. Lee, J. H. Kang and J. W. Choi, *ACS Appl. Mater. Interfaces*, 2024, **16**, 8930–8938.
35 P. Wang, B. Xi, Z. Zhang, N. Song, W. Chen, J. Feng and S. Xiong, *Small*, 2021, **17**, 2103744.
36 B. Liu, Y. Zhang, G. Pan, C. Ai, S. Deng, S. Liu, Q. Liu, X. Wang, X. Xia and J. Tu, *J. Mater. Chem. A*, 2019, **7**, 21794–21801.
37 S. Han, E.-H. Noh, S. Chae, K. Kwon, J. Lee, J.-S. Woo, S. Park, J. W. Lee, P. J. Kim, T. Song, W.-J. Kwak and J. Choi, *J. Energy Storage*, 2024, **96**, 112693.
38 H. L. Bui and A. de Klerk, *J. Chem. Eng. Data*, 2013, **58**, 1039–1049.
39 H. Xie, Y. Li and J. B. Goodenough, *Mater. Res. Bull.*, 2012, **47**, 1229–1232.
40 H. Arito and R. Soda, *Ann. Occup. Hyg.*, 1977, **20**, 247–255.
41 K. Kim, H. Ma, S. Park and N.-S. Choi, *ACS Energy Lett.*, 2020, **5**, 1537–1553.
42 Y. Kim, *J. Mater. Sci.*, 2013, **48**, 8547–8551.
43 Y. Sohn, J. Oh, J. Lee, H. Kim, I. Hwang, G. Noh, T. Lee, J. Y. Kim, K. Y. Bae, T. Lee, N. Lee, W. J. Chung and J. W. Choi, *Adv. Mater.*, 2024, **36**, 2407443.
44 Z. Lu, Z. Zhang, X. Chen, Q. Chen, F. Ren, M. Wang, S. Wu, Z. Peng, D. Wang and J. Ye, *Energy Storage Mater.*, 2018, **11**, 47–56.
45 J. Sun, Y. Cheng, H. Zhang, X. Yan, Z. Sun, W. Ye, W. Li, M. Zhang, H. Gao, J. Han, D.-L. Peng, Y. Yang and M.-S. Wang, *Nano Lett.*, 2022, **22**, 5874–5882.
46 D. Zhao, B. Ma, C. Wang, Y. Zhang, S. Shi and Y. Chen, *Chem. Eng. J.*, 2022, **433**, 133804.
47 W. Liu, Z. Chen, Z. Zhang, P. Jiang, Y. Chen, E. Paek, Y. Wang and D. Mitlin, *Energy Environ. Sci.*, 2021, **14**, 382–395.